PAPER

Experimental investigation and modeling of the temperature memory effect in a 4D-printed auxetic structure

To cite this article: Chiara Pasini *et al* 2022 *Smart Mater. Struct.* **31** 095021

IOP Publishing Smart Materials and Structures
Smart Mater. Struct. **31** (2022) 095021 (19pp) https://doi.org/10.1088/1361-665X/ac8031

Experimental investigation and modeling of the temperature memory effect in a 4D-printed auxetic structure

Chiara Pasini[1], Nicoletta Inverardi[1], Davide Battini[1], Giulia Scalet[2], Stefania Marconi[2], Ferdinando Auricchio[2] and Stefano Pandini[1,*]

[1] Department of Mechanical and Industrial Engineering, University of Brescia, via Branze 38, 25133 Brescia, Italy
[2] Department of Civil Engineering and Architecture, University of Pavia, via Ferrata 3, 27100 Pavia, Italy

E-mail: stefano.pandini@unibs.it

Received 22 April 2022, revised 21 June 2022
Accepted for publication 8 July 2022
Published 22 July 2022

Abstract
4D printing is an innovative manufacturing approach that combines 3D printing and stimuli-responsive abilities to produce objects with complex geometry and capable of shapeshifting over time (the fourth dimension). To pursue such an approach this paper proposes to develop re-entrant honeycomb auxetic grids with tunable shape reconfigurable behavior. Particularly, the work combines 3D printing and a photopolymer exhibiting the so-called temperature memory effect (TME), a peculiar shape memory behavior expressing the capability of the material to remember not only the original shape but also the deformation temperature. A thorough experimental activity was carried out on single auxetic unit cells, chosen as representative of the whole auxetic grid, to properly highlight and assess their response upon heating after single-step and multiple-step deformation histories and to describe the recovery process as a function of time and temperature. Results demonstrate the possibility to achieve an easily controlled TME and to successfully exploit it for autonomous, complex hierarchical transformations over a large range of temperatures. As a proof-of-concept, the study of the sequential recovery of an entire auxetic grid subjected to double-step programming allowed highlighting a decoupled in-plane elongation and out-of-plane bending. The behavior of the 4D-printed auxetic structures was simulated by means of finite element (FE) analysis, using a thermoviscoelastic model of the photopolymer and viscoelastic experimental data obtained by time-temperature superposition analysis applied to multifrequency dynamic mechanical tests and to isothermal recovery tests. A good correspondence between experiments and simulations was obtained for all shape memory tests, demonstrating that the proposed FE approach is a suitable tool to support the design of these structures. The combination of 3D printing and TME opens new perspectives to achieve dynamic tunability in mechanical metamaterials, that is a key ingredient in several application fields.

* Author to whom any correspondence should be addressed.

Supplementary material for this article is available online

Keywords: shape memory polymer, 4D printing, auxetic, metamaterial, temperature memory effect

(Some figures may appear in colour only in the online journal)

1. Introduction

Research on shape memory materials and structures found new stimuli in the beneficial combination with additive manufacturing (AM) technologies, aiming to obtain 3D-printed systems with the ability to change shape, function, or properties in response to an external stimulus. Such an approach was variously addressed in fundamental and applied research works, by properly choosing materials and stimuli, and all these attempts were grouped under the name 4D printing, the 4th dimension representing the 3D-printed object evolution over time [1–4].

In the pioneer work of Tibbits [5, 6], with the term 4D printing referred to systems that were ready to evolve in reaction to a stimulus directly off the print bed, mainly relying on multi-material printing, as a consequence of the mismatch between the coefficients of thermal or hygroscopic expansion of the materials. In other works [7, 8], an inherent shapeshifting attitude was obtained in structures composed of a single material by creating stress mismatch between layers printed with different anisotropic patterns.

The adoption of thermo-responsive shape memory polymers (SMPs) as base materials represents a further 4D printing strategy. Thermo-responsive SMPs are smart polymeric materials provided with a 'permanent' (or 'original') shape that can be set (or 'programmed') in a 'temporary' configuration, which may be kept until a specific thermal stimulus is applied and activates the return to the permanent shape. In particular, the effect is promoted by heating above a specific thermal region (typically around the glass transition temperature, T_g, or the melting temperature, T_m). Various were the attempts to create structures capable of changing their shape as a result of a specific thermo-mechanical history applied after the 3D printing process ('programming' was here treated as 'constrained-thermo-mechanics' [3, 4] or as a 'post-processing' step [1]). While requiring a further intervention after AM, this 4D printing approach is often regarded as a more common and versatile strategy towards a tailored and highly controlled shapeshifting ability [1, 3].

The realization of shape memory structures by means of AM technologies allows developing and studying objects with increased degree of complexity, focusing on their design rather than on realization issues. An interesting case is that of auxetic metamaterials. Auxetics exhibit the peculiar behavior of a negative Poisson's ratio (NPR), by which, unlike conventional materials, they tend to expand transversally upon longitudinal elongation, and, vice versa, contract transversally upon longitudinal compression [9]. This response is regarded with interest, as possibly leading to improved mechanical resistance, synclastic behavior upon flexure, higher energy/shock absorption, and variable permeability [10, 11]. Various applications may benefit from such a property profile [10–12]: protective systems for aerospace, defense, automotive and sport [13, 14]; smart sensors and actuators [15, 16]; biomedical foldable stents [17, 18] and smart bandages for controlled drug release [19]; novel fibers for textiles [20] and composites [21, 22]; fasteners with enhanced performance [23, 24].

The counterintuitive auxetic behavior stems from a peculiar geometrical structure, often obtained by repetition of small unit patterns (or 'cells') to large scale [25]. There are several types of configurations that may lead, to various extents, to the NPR behavior (re-entrant honeycombs; rotating polygonal structures; chiral structures; crumpled or perforated sheets; multi-material and composite structures), as widely covered and classified in several reviews [9, 10, 12, 26, 27]. Towards an optimization of the design of auxetic structures, analytical and finite element (FE) models have also been developed to predict the mechanical properties of auxetics based on the geometrical parameters of their cells [28–31].

For what regards 4D printing of auxetics, current research has two main objectives: (a) developing structures that may be programmed, and reversibly reconfigured, to tune their Poisson's ratio and stiffness upon changing the cell geometry [32–40]; (b) exploring possible uses of these smart metamaterials. Suggested applications include: structures that may be extraordinarily compacted/expanded and still be able to revert to their original shape on a thermal trigger [41]; sandwich panels with improved shock absorption possessing a recoverable structure [35, 42]; highly compliant structures, conceived for application in flexible/soft electronics [34, 37]; self-deployable biomedical devices such as stents [36] or scaffolds [34]; composite textiles with potential as smart, reinforced, and protective clothing [43].

In most of these works the shape memory response was governed by a single recovery process from a programmed to a permanent shape, promoted by heating above a temperature, whose value was dictated by the transition temperature of the material itself (i.e. its T_g or T_m). However, recent literature on 4D-printed structures based on SMPs aimed at an improved control of the shape evolution with temperature and time, in order to freely design non only the original and the temporary shapes, but also other features, such as the recovery temperature, the recovery rate, or the presence of multiple recovery steps occurring in a sequence. With this purpose, AM of polymers featuring a broad transition region represents a noteworthy approach, due to their so-called 'temperature memory effect' (TME). The TME may be described as the ability of a SMP to memorize not only the shape, but also the temperature at which it has been deformed [44, 45]. This behavior may be exhibited by both amorphous [44–50] and semicrystalline [51–55] polymers with either glass or melting transition distributed over a broad temperature range. The switching temperature of these SMPs may be precisely controlled by the applied thermo-mechanical history, with no need to modify the material synthesis to achieve a tunable shape memory effect [44, 50, 52–55]. Moreover, by deforming the material following a multi-step programming history, with each step carried out at a different temperature, it is possible to obtain more than one switching temperature and thus polymers capable of multiple shape memory effect and sequential motion ability [45–49, 51, 56, 57]. Despite the versatility of this approach with respect to more complex strategies towards multiple/sequential shape memory (multi-material printing [58–61]; functionally graded structures [62–64]; SMPs displaying multiple transition temperatures [65–67]), only few works focused on 4D printing of polymers exhibiting the TME. These studies experimentally confirmed the suitability of the TME of photo-crosslinked polymers to provide sequential motions, both for simple geometries (bards under bending [46]; cubes under compression [47]) and for more complex structures (truss structures [46]; self-locking clamps [47]; single auxetic cells exhibiting decoupled in-plane and out-of-plane motion [48]).

Considering the complex shape transformations that may be obtained by 3D printing materials exhibiting the TME, the support of FE analysis is considered a fundamental tool to properly program and simulate the response of these materials. The most simple and common approach to predict the response of SMPs is based on thermo-viscoelastic constitutive models. According to these models, the ability to fix/recover a given strain is based on the viscosity changes of rheological elements in the model. By this point of view, materials exhibiting the TME, are not dissimilar from the most standard SMPs, but they require a finer characterization of the model parameters in order to properly describe their highly distributed thermal transition process. For this reason, a generalized Maxwell model with multiple non-equilibrium branches is often employed [46, 56, 57, 68, 69]. This approach offered the possibility of theoretically describing the response of materials presenting the TME and of predicting it according to specific programming parameters (i.e. deformation temperature, deformation, holding and cooling time) and heating histories. A good agreement was found for various materials (Nafion perfluorosulfonic acid ionomer [56, 57, 68]; acrylate-based amorphous polymer [69]; epoxy based photo-curable resin [46]) and thermomechanical histories. Interestingly, in the works of Yu *et al* [56, 69] a mechanistic description of the model accompanies the simulations, offering an explanation of the TME principle in terms of a different storage of stress or, equivalently, elastic strain energy in equilibrium and non-equilibrium branches of the thermoviscoelastic model. However, most of the experiments involved only simple rectangular specimens subjected to tensile or bending conditions and recovering their original shape upon continuous or segmented thermal ramps.

In the present work, we developed smart 4D-printed structures by simultaneously exploiting AM technologies, to produce them with a complex shape (auxetic metamaterial), and the TME, to achieve complex shape changes (multiple/sequential shapeshifting). We employed a commercial photopolymer and a thermoviscoelastic model available in most commercial FE analysis software, so that the presented approach may be easily replicated experimentally and numerically. To the best of our knowledge, with respect to the current literature on 4D printing, this is the first work in which the sequential motion of 4D-printed auxetic structures is tailored on the basis of the TME and numerically simulated. More specifically, the shape memory auxetic structure is realized by means of vat photopolymerization with a stereolithographic apparatus (SLA), starting from a commercial photopolymer featuring a broad glass transition [47]. Its shape memory response is investigated upon application of single- and multi-step programming, in order to highlight the peculiarities of the TME and the chance of exploiting it towards the achievement of a tunable thermal triggering as well as multiple and sequential recovery processes under uniaxial and multiaxial conditions. The TME is studied via experiments carried out as a function of temperature along controlled heating ramps, in the so-called thermally stimulated recovery (TSR) tests, and as a function of time, in isothermal recovery experiments. Starting from the thermo-mechanical properties measured by dynamic mechanical analysis (DMA), an FE model based on a thermoviscoelastic approach is developed, and the reliability of the model is tested by comparing its prediction with experimental results. Finally, the TME is tested on an auxetic grid, demonstrating the feasibility of achieving sequential motions in an additively manufactured structure consisting of a single material.

2. Experimental

2.1. AM of auxetic structures

The auxetic structure investigated in the present work had a re-entrant honeycomb geometry, with dimensions specified in figure 1. Its auxetic behavior was verified in a previous work by the authors [48] and resulted in a Poisson's ratio of -0.18.

The specimens featuring this structure were produced by vat photopolymerization, with the SLA Formlabs Form 2, following the protocol described in [48]. The photopolymer resin named Clear FLGPCL02, formulated and provided by Formlabs company as a mixture of methacrylic acid esters and photoinitiator in a liquid physical state, that could be turned into solid by exposition to UV light, was used.

2.2. Thermal and mechanical analyses

DMA was performed by means of a DMA Q800 analyzer (TA Instruments) on a bar-shaped specimen obtained by the same SLA (13–14 mm long; cross-section: 1 mm $\times$ 0.8 mm). The specimen was tested under tensile configuration (applied displacement amplitude equal to 15 μm) and multi-frequency mode (frequency sweeps from 0.3 Hz to 150 Hz), scanning a temperature range from -40 °C to 120 °C at 0.5 °C min^{-1}. The heating rate was kept low to recreate nearly isothermal conditions during each frequency sweep.

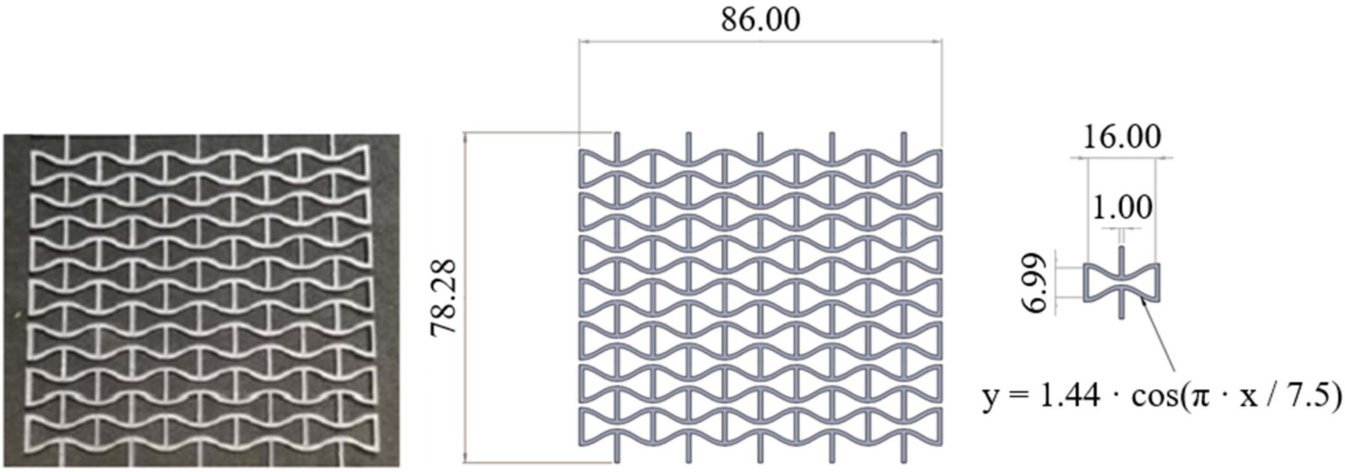

Figure 1. Re-entrant honeycomb auxetic grid by vat photopolymerization and its CAD model, reporting the dimensions of the grid and of the repeating unit cell in mm (thickness = 0.8 mm). The equation refers to the auxetic cell profile, *y* being the vertical direction and *x* the horizontal one.

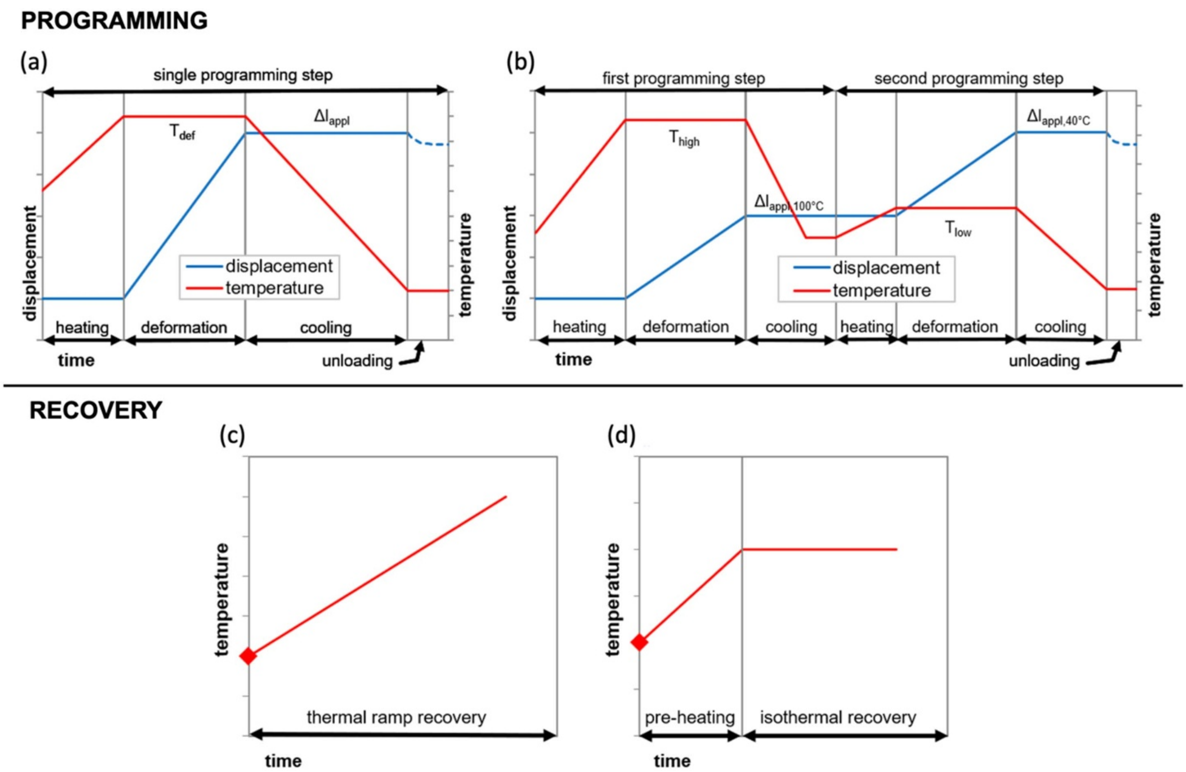

Figure 2. Representation of the thermo-mechanical histories applied to the auxetic cells during single-step programming (a), double-step programming (b), recovery upon a thermal ramp (c) and isothermal recovery (d).

2.3. Shape memory tests

The shape memory behavior was characterized through various thermo-mechanical histories, which consisted in the combination of different types of programming and recovery steps, schematically summarized in figure 2. The programming phase consisted of either a single step or a double step, whereas the activation of the shape memory occurred either upon a thermal ramp, in the so-called TSR tests, or upon a constant temperature, in isothermal recovery tests. All these tests were carried out on single auxetic cells by means of a DMA analyzer (DMA Q800—TA Instruments), under tensile configuration.

2.3.1. TSR tests with single-step programming. The first TSR tests consisted of a single-step programming phase (figure 2(a)) followed by recovery upon a heating ramp (figure 2(c)). More in detail, the thermo-mechanical history applied during programming is the following:

(a) heating up to a given deformation temperature T_{def};
(b) applying a tensile elongation of 3.5 mm (i.e. a displacement close to maximum cell opening condition);
(c) cooling to −15 °C under fixed strain conditions (i.e. by maintaining fixed the clamp distance);
(d) unloading.

The programming phase was carried out at different values of T_{def}, namely 20 °C, 40 °C, 60 °C, 80 °C and 100 °C, and the cooling temperature (−15 °C) was selected well below the glass transition temperature, within the glassy region, which may be considered a stable thermal region for what concerns shape fixation because chain mobility is practically suppressed. Then, the recovery phase occurred upon heating at 1 °C min^{-1} up to 110 °C, under quasi stress-free condition (i.e. application of a moderate constant load, equal to 0.001 N), in order to continuously monitor the cell displacement as a function of temperature.

Under tensile conditions, the cell segments underwent different types of strain (axial and flexural), with values varying from point to point for a same degree of cell opening, so that the global cell deformation could not be described in terms of nominal strain. Moreover, the DMA analyzer could only measure the overall elongation/contraction of the cell, but not the local strain values, due to its closed chamber. Therefore, all the shape changes of the specimens were represented as a function of temperature in terms of normalized displacement, Δl_{norm}, defined as:

$$\Delta l_{norm}\,[\%] = (\Delta l/\Delta l_{appl}) \times 100, \quad (1)$$

where: $\Delta l = l - l_0$; $\Delta l_{appl} = l_{appl} - l_0$; l is the distance between the clamps during the test; l_0 is the initial clamp distance; l_{appl} is the clamp distance corresponding to the applied elongation. The distribution of the process was described through the temperature derivative of the normalized displacement, here called recovery rate (RR_T) and defined as:

$$RR_T\,[\%\,°C^{-1}] = d(\Delta l_{norm})/dT. \quad (2)$$

In addition, the following parameters were employed to further describe the shape memory response:

(a) strain fixity (SF), i.e. the percentage of deformation that is fixed in the specimen after load removal, which was defined as:

$$SF\,[\%] = (\Delta l_{unload}/\Delta l_{appl}) \times 100, \quad (3)$$

where: $\Delta l_{unload} = l_{unload} - l_0$; l_{unload} is the clamp distance at load removal;

(b) strain recovery (SR), i.e. the percentage of deformation that was recovered at the end of the heating ramp, which was defined as:

$$SR\,[\%] = [1 - (\Delta l_{final}/\Delta l_{appl})] \times 100, \quad (4)$$

where: $\Delta l_{final} = l_{final} - l_0$; l_{final} is the clamp distance at the end of the test.

2.3.2. TSR tests with multi-step programming. Further analyses of the sample by TSR tests aimed at exploring the possibility of obtaining a multiple shape memory response upon application of a double-step programming (figure 2(b)). In this case, the specimens were programmed as follows:

(a) heating from room temperature up to $T_{high} = 100$ °C;
(b) applying a first tensile elongation $\Delta l_{appl,100\,°C}$;
(c) cooling to 20 °C under fixed strain conditions;
(d) heating up to $T_{low} = 40$ °C;
(e) applying an additional tensile elongation $\Delta l_{appl,40\,°C}$;
(f) cooling to −15 °C under fixed strain conditions;
(g) unloading.

The total applied displacement was kept constant (i.e. $\Delta l_{appl} = 3.5$ mm), and the partial displacements, $\Delta l_{appl,100\,°C}$ and $\Delta l_{appl,40\,°C}$, were expressed as percentages with respect to the total displacement (25% $\Delta l_{appl} \approx 0.875$ mm; 50% $\Delta l_{appl} \approx 1.75$ mm; 75% $\Delta l_{appl} \approx 2.625$ mm). Three different ratios between the partial displacements were employed and indicated as couples of percentages (25%–75%; 50%–50%; 75%–25%), with the first value referred to the deformation step at T_{high} and the second one referred to the deformation step at T_{low}. The recovery stage remained unchanged (figure 2(c)).

2.3.3. Isothermal recovery tests. Isothermal recovery tests were carried out on single auxetic cells by means of the DMA analyzer, under tensile configuration.

The isothermal approach hereby discussed differs from the previous TSR approach in the recovery stage only (figure 2(d)). The tests were carried out on specimens programmed under various single-step (figure 2(a)) and two-step (figure 2(b)) thermo-mechanical histories:

(a) single-step tensile deformation for a displacement equal to 3.5 mm at $T_{def} = 40$ °C;
(b) single-step tensile deformation for a displacement equal to 3.5 mm at $T_{def} = 100$ °C;
(c) double-step tensile deformation equal to 3.5 mm (50% at $T_{high} = 40$ °C and 50% at $T_{low} = 100$ °C).

The recovery was performed under quasi stress-free conditions (0.001 N applied load) at a constant recovery temperature, T_{rec}, and monitored as a function of time. Different values of T_{rec}, between −20 °C and 85 °C, were tested. More specifically, for each T_{rec} the thermal program in the recovery step consisted of a first heating at 5 °C below T_{rec}, then slowly approaching T_{rec} at 1 °C min^{-1}, and finally maintaining T_{rec} for 60 min. The various heating stages were specifically conceived so to obtain an adequately fast transitory regime from the initial temperature to T_{rec}, while avoiding temperature overshooting.

The recovery response under isothermal condition was described in terms of normalized displacement, Δl_{norm}, as a function of time, and in terms of recovery rate, $\mathrm{RR_t}$, evaluated as the derivative of Δl_{norm} with respect to the logarithm of time:

$$\mathrm{RR_t}\,[\%] = \mathrm{d}(\Delta l_{\mathrm{norm}})/\mathrm{d}(\log t). \tag{5}$$

The starting point of each isothermal recovery curve was taken when the specimen was considered being at equilibrium at T_{rec}, at the end of the slower heating stage (i.e. when a thermally stationary condition is reached).

The isothermal curves were also used for the construction of recovery master curves of the normalized displacement along time, mutually shifting the curves on the basis of a time-temperature superposition scheme and choosing a reference temperature T_0 equal to 25 °C.

2.4. Numerical simulations

FE simulations were carried out with the commercial software DS Simulia Abaqus 2020. The TME effect was implemented by defining a visco-hyperelastic behavior [70–75] which consists of three different contributions:

(a) a hyperelastic strain energy function to fit the time-independent (fully relaxed) non-linear static behavior of the material;
(b) a generalized Maxwell model to enrich the hyperelastic response with time dependency;
(c) a William–Landel–Ferry (WLF) equation which introduces temperature dependency through the definition of a time-temperature correlation.

More specifically, a fully incompressible Neo-Hookean strain energy density (U) was considered to describe the hyperelastic behavior as reported in the following equation:

$$U = 0.5\,G_\infty\,\left(\overline{I_1} - 3\right) \tag{6}$$

where G_∞ is the initial relaxed shear modulus and $\overline{I_1}$ is the first deviatoric strain invariant; the value of G_∞ was obtained from the modulus values of the rubbery plateau measured in DMA tests.

The generalized Maxwell model [76, 77] describes the relaxation of the complex dynamic modulus G^* as $G^* = G' + iG''$ where G' is the storage modulus and G'' is loss modulus. The linear viscoelasticity introduced with this model was then implemented in the FE software with the definition of a Prony series [78] as reported below:

$$G'(\omega) = G_0\left(1 - \sum_{i=1}^{N} g_i + \sum_{i=1}^{N}\frac{g_i\tau_i^2\omega^2}{1+\tau_i^2\omega^2}\right) \tag{7}$$

$$G''(\omega) = G_0\sum_{i=1}^{N}\frac{g_i\tau_i\omega}{1+\tau_i^2\omega^2} \tag{8}$$

where G_0 is the instantaneous modulus, ω is the angular reduced frequency and (g_i, τ_i) are the coefficients of the Prony series with g_i being dimensionless and τ_i having the dimensions of ω^{-1}. The custom optimization routine provided in [79] was used to fit DMA data and find the optimal (g_i, τ_i) values. G_0 was obtained from DMA data as well.

The WLF equation allows switching from temperature to time domain through the so-called shift factors $a_{T_0}^{T}$ via equation (9):

$$\log\left(a_{T_0}^{T}\right) = \frac{-C_1\,(T - T_0)}{C_2 + (T - T_0)} \quad \text{with } f_R = a_{T_0}^{T} f \text{ and } \omega = 2\pi f \tag{9}$$

where C_1 is a dimensionless coefficient, C_2 is a coefficient with dimensions of temperature, T_0 is the reference temperature set at 25 °C, T is the temperature associated with the shift factor $a_{T_0}^{T}$ and f_R and f are, respectively, the reduced frequency and the DMA data frequency.

Two shift factor data sets were experimentally obtained: one by the construction of master curve from multi-frequency DMA; the other by the construction of recovery master curves from isothermal recovery tests. A nonlinear least squares method was used to find optimal values of WLF parameters for both shift factor data sets.

2.4.1. FE model setup. The FE model was setup to reproduce the experimental configuration for all the shape memory tests described in section 2.3. Since in this configuration only a single cell was used, three symmetry planes could be exploited to reduce the modeled geometry to 1/8th and proper boundary conditions were applied to all the faces along the symmetry planes (figure 3). Specifically, on each surface belonging to a symmetry plane, any out-of-plane translation was constrained and thus: (a) each node lying on the X-plane symmetry face resulted fixed with respect to the X translation and the Y and Z rotations; (b) each node lying on the Y-plane symmetry face resulted fixed with respect to the Y translation and the X and Z rotations; (c) each node lying on the Z-plane symmetry face resulted fixed with respect to the Z translation and the X and Y rotations.

The mesh consisted of 504 s order hexahedral elements with linear temperature, hybrid formulation and reduced integration (Abaqus label C3D20RHT) to ensure an accurate representation of stress gradients and to maintain limited computational times considering the high number of simulations that had to be performed.

The loading and thermal histories replicated the experimental test data by following the qualitative representation shown in figure 2. Heat transfer was also included in the simulation to take into consideration any possible effect of thermal inertia by applying typical values for thermal conductivity, specific heat, and free air convection coefficient (values were conveniently defined as follows: thermal conductivity = 0.2 W m^{-1} K^{-1}, specific heat = 1466 J kg^{-1} K^{-1}, air convection coefficient = 10 W m^{-2} K^{-1}.

In the end, the results of simulated recovery tests were compared to those of the corresponding experimental tests.

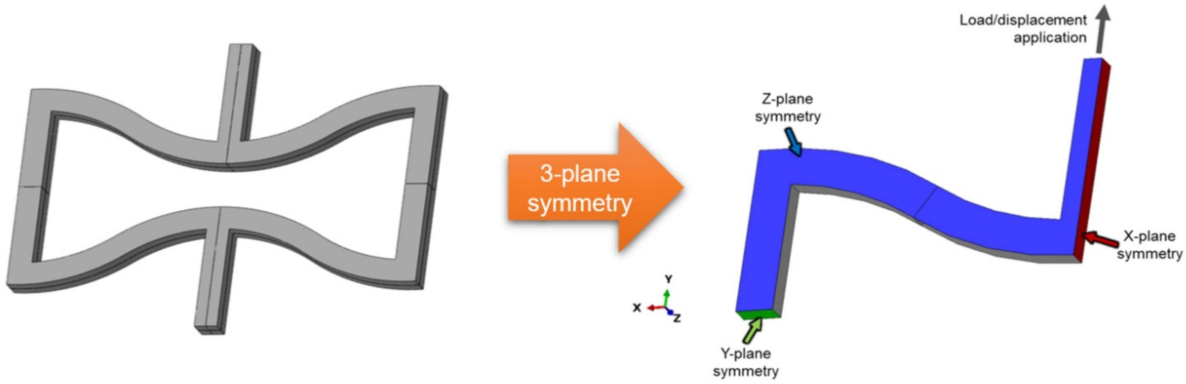

Figure 3. Three-plane symmetry and boundary conditions applied in the FE model of the auxetic unit cell.

2.5. Sequential recovery of in-plane and out-of-plane deformations for an auxetic grid

The possibility of a sequential shape recovery was evaluated on an auxetic grid by applying sequential in-plane (tensile) and out-of-plane (bending) deformation. The specimen was subjected to a double-step programming followed by recovery in a heated bath, according to the following thermo-mechanical history:

(a) heating from room temperature up to $T_{high} = 100$ °C inside the heating chamber of an electromechanical dynamometer (Instron mod. 3366);
(b) applying a tensile elongation of 10 mm (i.e. a displacement close to maximum cell opening condition) with a crosshead speed of 1 mm min^{-1};
(c) cooling down to room temperature under fixed strain conditions;
(d) heating up to $T_{low} = 40$ °C inside a lab oven while still keeping fixed the first temporary shape applied;
(e) bending the grid around a 30 mm diameter tube and fixing the deformation with rubber bands;
(f) cooling down to 5 °C under fixed strain conditions in a refrigerator;
(g) removal of the grid from the tube and subsequent heating in a water bath placed on a hot plate from about 24 °C to 63 °C (30 min at about 1 °C min^{-1} followed by 30 min at about 0.25 °C min^{-1}).

The recovery was monitored with two cameras, one recording the top view and one recording from the side view of the bath.

Afterwards, the FE model was set up to reproduce the experimental testing sequence. Since the testing required out-of-plane displacements and different boundaries at the axial ends, only one symmetry plane could be used. Figure 4 shows the symmetry plane and the boundary and loading conditions.

The mesh consisted of more than 34 000 first order hexahedral elements with hybrid formulation and reduced integration (Abaqus label, C3D8RHT). The loading and thermal histories replicated the experiment. Heat transfer was also included in the simulation to take into consideration possible thermal inertia effects by applying free air and water convection interactions (specifications are referenced in section 2.4, with the additional water convection coefficient being assumed an order of magnitude higher than the air convection coefficient).

The comparison between experimental and simulated recovery was carried out by considering the evolution of two dimensions of the grid along the heating ramp, described as:

(a) normalized elongation of three cells at the center of the grid ΔL_{norm},

$$\Delta L_{norm}\,[\%] = (\Delta L/\Delta L_{appl}) \times 100, \tag{10}$$

where: $\Delta L = L - L_0$; $\Delta L_{appl} = L_{appl} - L_0$; L is the overall length of the three auxetic cells as shown on the left in figure 4; L_0 is the value of L before elongation; L_{appl} is the value of L after elongation;

(b) normalized end-to-end distance of the whole grid, ΔW_{norm},

$$\Delta W_{norm}\,[\%] = (\Delta W/\Delta W_{appl}) \times 100, \tag{11}$$

where: $\Delta W = W - W_0$; $\Delta W_{appl} = W_{appl} - W_0$; W is the end-to-end distance along the X direction as shown on the left in figure 4; W_0 is the value of W before bending; W_{appl} is the value of W after bending.

3. Results and discussion

3.1. Thermal and mechanical analyses

The resin exhibits a broad glass transition region, which is a key requirement for the TME. In fact, differential scanning calorimetry allowed detecting a transition process approximately distributed between −20 °C and 80 °C, as described in section S1 of the supplementary material (figure S1(a)). The temperature interval of the transition region was also confirmed by DMA traces, which suggest a glass transition temperature (T_g) between 25 °C and 30 °C, as estimated at the loss modulus peak (figure S1(b)).

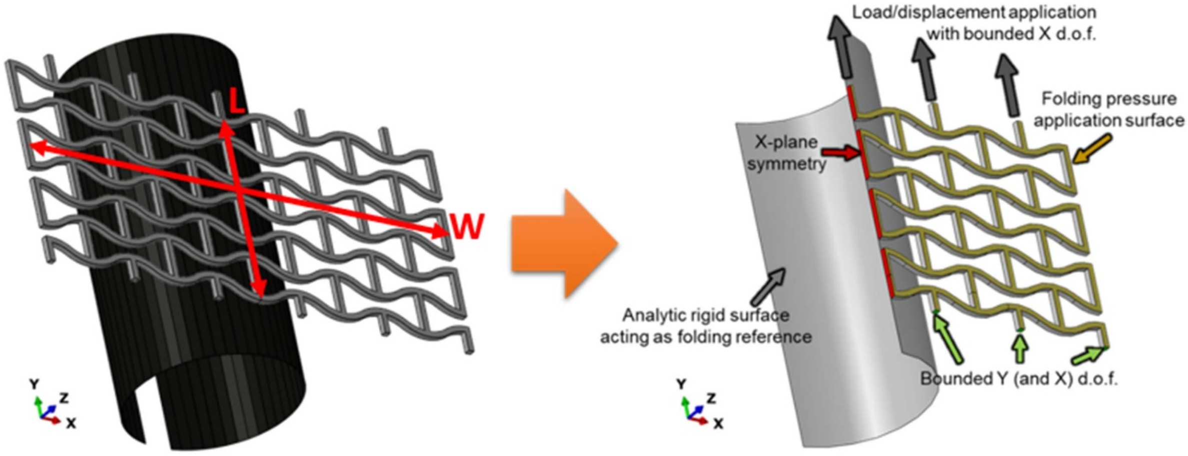

Figure 4. On the left: the elongation (L) and projected width (W) used for equations (10) and (11) are shown. On the right: the boundary conditions and loadings applied in the FE model of the auxetic grid are highlighted.

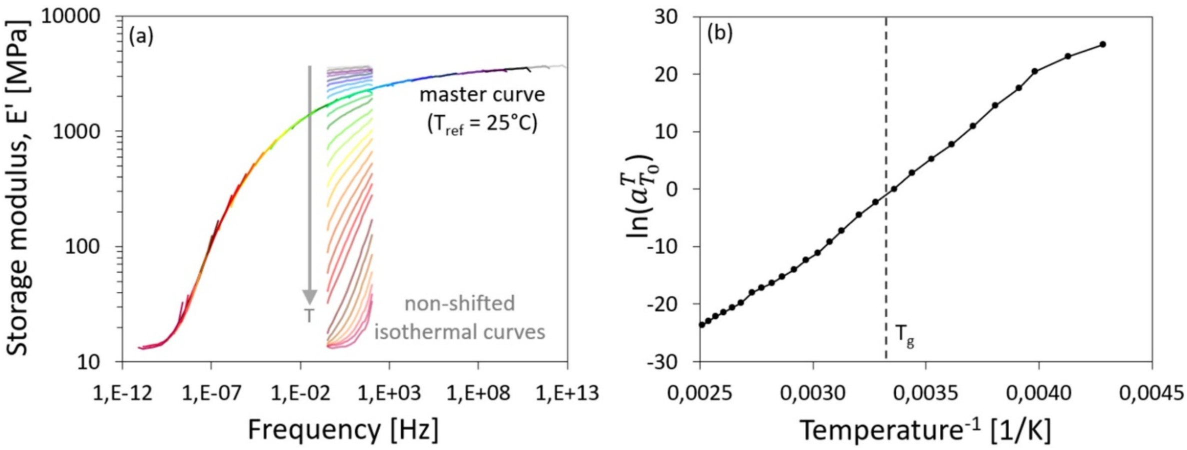

Figure 5. (a) Non-shifted isothermal curves (pale stacked curves between 10^{-2} Hz and 10^{2} Hz) and master curve of the storage modulus (vivid overlapped curves) as a function of frequency, for a reference temperature T_0 equal to 25 °C; (b) relationship between shift factors and temperature.

The results of the multifrequency DMA characterization are shown as a function of frequency in figure 5(a): isothermal frequency sweeps are reported as pale curves between 10^{-2} Hz and 10^{2} Hz, while the storage modulus master curve is composed by the vivid curves. Adopting 25 °C as reference temperature, T_0, and according to a time-temperature superposition scheme, the isothermal curves were rigidly shifted along the temperature axis until best superposition. This procedure allowed to obtain the storage modulus master curve, which provided information and data for the viscoelastic model of the material. The shift factors, $a^{T}_{T_0}$, employed in the master curve construction are represented in figure 5(b) as a function of $1/T$ (T being the absolute temperature), and they were used to describe the time-temperature dependence in the thermoviscoelastic model.

Additionally, a local strain analysis was accomplished via digital image correlation (DIC) to have insight into the local strain field of re-entrant honeycomb structures subjected to tensile stress. The auxetic grid mainly responded to the applied stress with the bending of the cell segments arranged perpendicularly to the load direction, with small local strain values that guaranteed the absence of complex phenomena such as yielding or highly non-linear creep effects (figure S2(a)), and accordingly with the DIC results on similar auxetic cells by Yousuf *et al* [33]. Moreover, the deformation mode of the grid was overall similar to that of a single auxetic cell (figure S2(b)), so that the results of shape memory tests on single auxetic cells are reasonably expected to be similar to those that would be found by testing the whole grid. More details on experiments and results are provided in section S2 of the supplementary material.

3.2. TSR tests

The results of TSR tests with a single-step programming were reported in figure 6(a) in terms of normalized displacement (i.e. the percentage of actual strain with respect to the applied strain) as a function of temperature along the recovery heating ramp. In addition, figure 6(b) displays the recovery rate traces (i.e. the temperature derivatives of the normalized

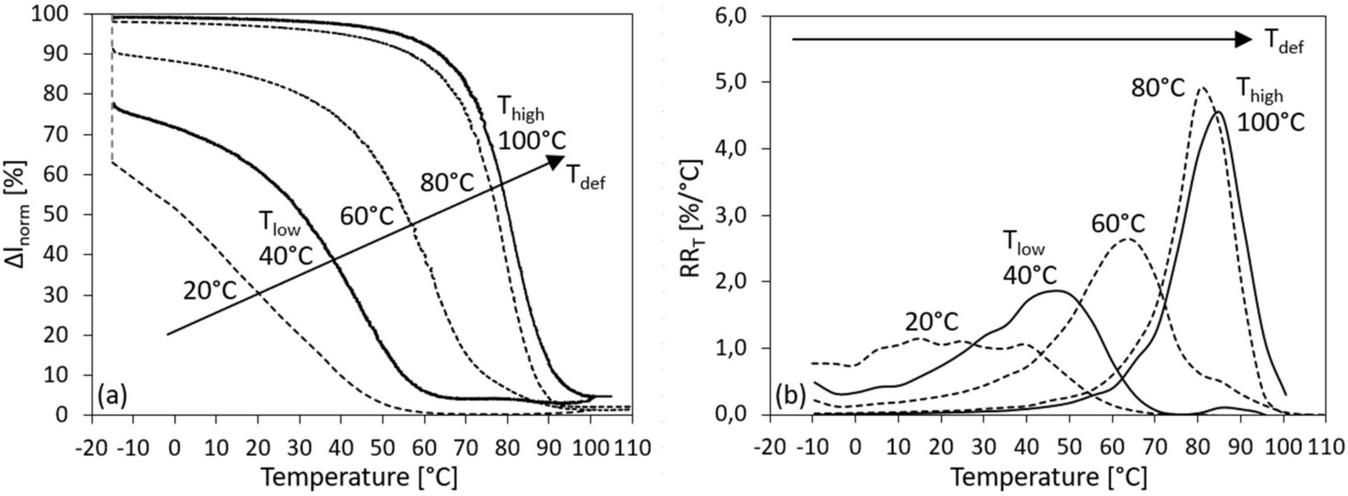

Figure 6. Normalized displacement, Δl_{norm} (a), and recovery rate, RR_T (b), as a function of temperature for TSR test with a single programming step, performed at various deformation temperatures T_{def}.

Table 1. Values of strain recovery, strain fixity and peak temperature T_{peak} for TSR tests with programming occurring at deformation temperature T_{def}.

TSR test	T_{def} (°C)	Strain recovery, SR (%)	Strain fixity, SF (%)	T_{peak} (°C)
Single-step programming	20	100	63	25
	40	97	77	47
	60	99	90	64
	80	98	98	81
	100	95	99	85
Double-step programming	100 (25%)–40 (75%)	100	84	50; 85
	100 (50%)–40 (50%)	94	88	45; 85
	100 (75%)–40 (25%)	94	92	47; 90

displacement curves), which are helpful in further describing the recovery process distribution. Each of the reported curves refers to a specimen deformed at a different deformation temperature, T_{def}. The results were also reported in table 1 in terms of SF, strain recovery, and T_{peak}, i.e. the peak temperature of the recovery rate process.

The material exhibited a good shape memory response (SR = 95%–100%) and the TSR approach evidenced the effects of T_{def} on the shape recovery. In fact, the recovery process distribution and location moved towards higher temperatures as T_{def} increased, according to the typical phenomenology of the TME. Moreover, SF showed excellent values for temperatures above 60 °C (i.e. at least 30 °C above T_g), while lower, but still significant, fixity values were found for lower temperatures. By contrast, strain recovery was not affected by the deformation temperature and all the auxetic cells recovered their original shape almost completely independently of T_{def}.

Moreover, as the deformation temperature increased, the recovery process shifted to higher temperatures and became narrower but more intense, with a higher recovery rate peak. This peak was considered as a characteristic recovery temperature, named as T_{peak} in table 1, and it showed a regular dependence on T_{def} assuming values close to T_{def} + 5 °C, except for the case of the highest deformation temperature explored, in which T_{def} = 100 °C and T_{peak} = 85 °C. Such correlation between T_{def} and T_{peak} can be ascribed to the fact that the resin actually exhibits the TME when deformed at T_{def} within its wide glass transition region (between −20 °C and 80 °C). In fact, the glass transition of the resin as a whole can be regarded as a broad distribution of relaxation sub-processes occurring at different temperatures. For this reason, the sub-processes with a transition temperature lower than T_{def} are the only ones responsible for the temporary shape fixation and, therefore, the recovery is promoted by temperatures above T_{def}, that is when all the interested sub-processes are activated. When the deformation temperature T_{def} overcomes the upper limit of the glass transition of the resin (80 °C) all recovery sub-processes are fully activated leading to an almost negligible sensitivity to further T_{def} changes, as could be appreciated from the TSR test at T_{def} = 100 °C.

Since the TME can be exploited to promote the auxetic cell shape recovery at specific temperatures, TSR tests with multi-step programming were carried out to investigate the possibility of a sequential recovery, controlling the temperature at which each single movement occurs. To this aim, two proper values of T_{def} had to be selected to ensure well separated recovery steps. T_{def} equal to 20 °C was excluded due to poor SF, so the best separation between recovery rate peaks (figure 6(b)) was found for T_{def} = 40 °C (thereafter called T_{low}) and T_{def} = 100 °C (thereafter called T_{high}). During

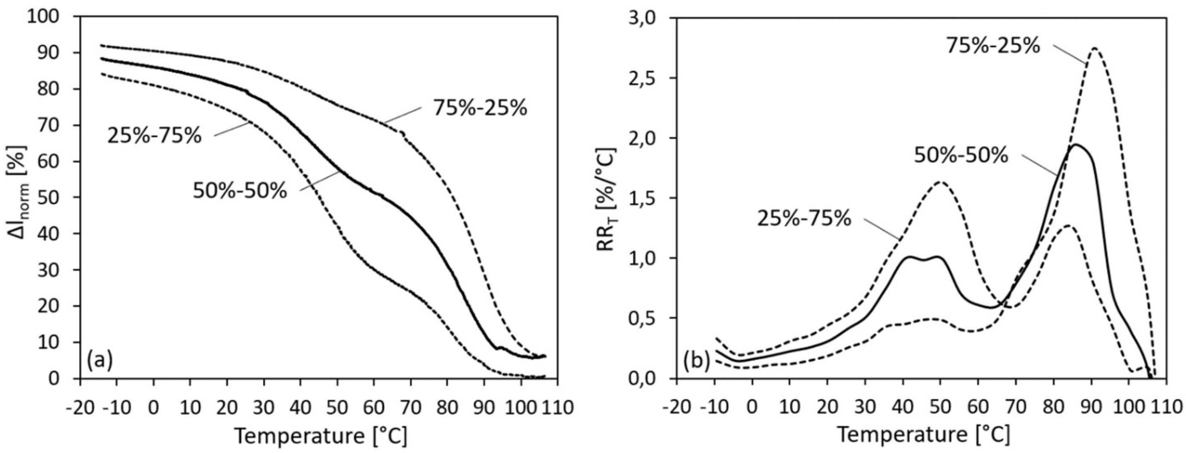

Figure 7. Normalized displacement, Δl_{norm} (a), and recovery rate, RR_T (b), as a function of temperature for TSR tests with a double-step programming, for different deformation histories (curves labeled as couples of percentage values with respect to the total applied displacement, the first value referred to the first deformation step at $T_{high} = 100$ °C, the second one to the second deformation step at $T_{low} = 40$ °C).

the first programming step, a tensile elongation $\Delta l_{appl,100\,°C}$ (equal to 25%, 50% or 75% of the total applied displacement) was applied at T_{high}, whereas in the second programming step the remaining deformation was applied at T_{low} with a second tensile elongation $\Delta l_{appl,40\,°C}$ (equal to 75%, 50% or 25% of the total applied displacement, respectively). The results of these multi-step programming tests were reported in figure 7 in terms of normalized displacement (a) and recovery rate (b) as a function of temperature.

All the specimens exhibited a good shape memory behavior, with high values of strain recovery and SF (see table 1). A double-step recovery is evidenced by two inflection points in the normalized displacement curves and two peaks in the recovery rate curves. Consistently with previous findings, the SF values ranged between those observed for TSR tests with single-step programming at 40 °C (SF = 77%) and 100 °C (SF = 99%). More precisely, the higher the elongation applied at 100 °C, the higher the SF. The correlation between T_{def} and T_{peak} was also confirmed: the deformation applied at 40 °C was mainly recovered around 45 °C–50 °C, while the recovery of the strain applied at 100 °C occurred at maximum rate slightly above the glass transition region, around 85 °C–90 °C, as reported in table 1. The TME allowed controlling not just the characteristic temperatures of both recovery steps, but also each step extent, since their relative proportion appeared to be the same as the proportion between the corresponding deformation steps. This principle can be exploited to design 4D-printed objects with complex sequential motions, and a good control of the shape change in each recovery step should be reasonably expected.

3.3. Isothermal recovery tests

Isothermal recovery tests allowed studying the recovery process of auxetic cells as a function of time at various temperatures. In fact, current literature typically investigated the TME for single and multi- step programming by adopting heating ramps at constant heating rate [44, 48–51, 53–55, 57, 68, 69]or segmented heating ramps [46, 49, 56, 57] comprising isothermal steps between ramp segments. In none of the cases a purely time-dependent description of the process could be obtained: in the case of single step programming, the distribution of the recovery process as a function of time is obviously influenced by the heating rate; in the case of multi-step programming, the degree of separation between the various recovery steps may strongly depend on the duration of the isothermal steps in-between the heating ramp segments. In order to describe the recovery as a pure function of time at a given temperature, an alternative approach is here proposed, adopting several isothermal experiments and a final representation of their results in terms of strain recovery master curve, obtained through the application of the time-temperature superposition principle.

The shape memory behavior was examined on specimens that were deformed either in a single-step programming (for two deformation temperatures: $T_{low} = 40$ °C and $T_{high} = 100$ °C) or in a double-step programming (specimens deformed in two steps: 50% Δl_{appl} at T_{high} and 50% Δl_{appl} at T_{low}). In this scenario, various recovery temperatures, ranging between −20 °C and 85 °C (i.e. approximatively across the glass transition region), were then explored.

Each isothermal recovery experiment included an early stage during which a non-isothermal transient recovery took place, while approaching T_{rec}. Examples of complete recovery curves can be observed in figure 8(a), where the normalized displacement is plotted against the total recovery time and the non-isothermal segments are represented by dashed lines. However, in the remaining graphs of figure 8 the curves refer only to the purely isothermal part of the experiment: thus the normalized displacement is represented as a function of isothermal recovery time, with the time origin being set to the instant of thermal equilibrium at T_{rec}. The isothermal curves are reported for specimens programmed at T_{low} (figure 8(b)), for specimens programmed at T_{high} (figure 8(c)), and for specimens programmed in two steps (50% at T_{high} and 50% at T_{low}; figure 8(d)).

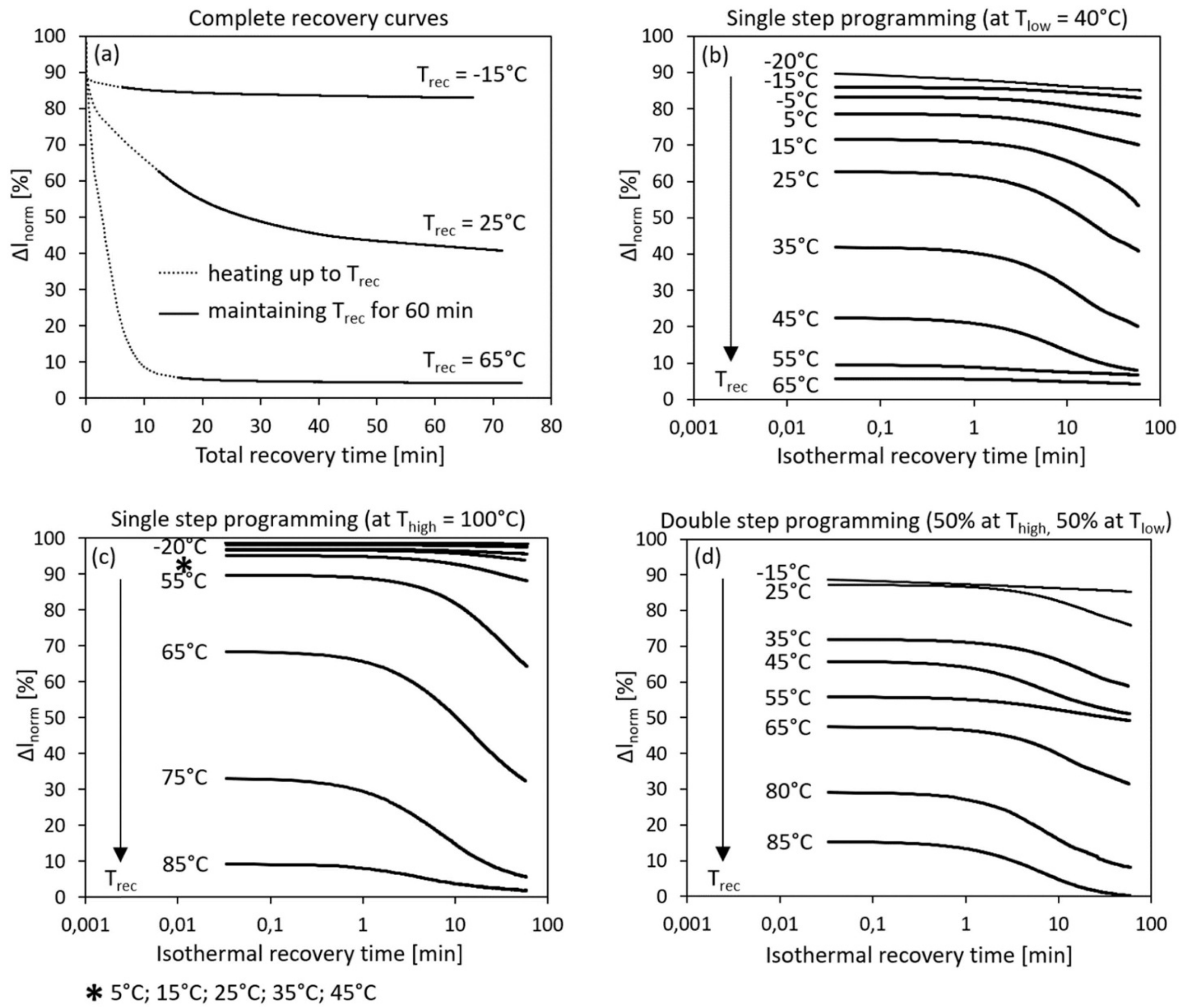

Figure 8. (a) Complete recovery curves reporting normalized displacement, Δl_{norm}, as a function of total recovery time, for specimens deformed at 40 °C and tested under isothermal conditions at three arbitrarily chosen recovery temperatures (T_{rec}). (b)–(d) Isothermal curves reporting Δl_{norm} as a function of isothermal recovery time, for specimens programmed at $T_{low} = 40$ °C (b), specimens programmed at $T_{high} = 100$ °C (c) and specimens programmed in two steps (50% at T_{high}, 50% at T_{low}) (d); the selected recovery temperatures T_{rec} are reported in each graph.

As time passed, the thermal stimulus promoted the shape recovery and the normalized displacement, Δl_{norm}, decreased, with a larger strain recovery being achieved for higher recovery temperatures. In particular, for each deformation temperature, the traces could be sorted into three representative trends, as displayed in figure 8(a): (a) for the lowest values of T_{rec}, the recovery was limited, with Δl_{norm} showing a nearly constant trend above 80%–90%; (b) as T_{rec} approached the deformation temperature, the isothermal curves assumed a sigmoidal shape and the specimens exhibited a significant recovery within 60 min under isothermal conditions; (c) finally, for higher recovery temperatures, most of the strain was recovered while heating up to T_{rec}, therefore Δl_{norm} was almost constant and lower than 10%.

These three trends were observed in all three experimental sets of figures 8 (b)–(d), independently from the programming history. However, a clear effect of T_{def} may be evidenced by comparing the behavior of auxetic cells programmed at T_{low} (figure 8(b)) and T_{high} (figure 8(c)): considering the same T_{rec}, the recovery process of the specimens deformed at the lowest temperature was in a more advanced state. Particularly, maintaining the cells at 45 °C allowed completing the recovery within 60 min for $T_{def} = T_{low}$, whereas a recovery temperature of 75 °C was required for $T_{def} = T_{high}$. Interestingly enough, these temperature values recall the characteristic recovery temperatures of TSR tests (47 °C for T_{low} and 81 °C for T_{high}).

When a double-step programming was applied (figure 8(d)), the existence of two distinct recovery steps was well emphasized both by the presence of two series of sigmoidal curves at about 25 °C–45 °C and 65 °C–85 °C, and by the presence of a temperature region in-between at about 55 °C where no significant recovery occurs. This behavior can also be regarded as the first recovery step being almost completed at around Δl_{norm} = 50%–60% while the second one having yet to start.

At this point, recovery master curves were developed to achieve a better understanding of the time scale of the

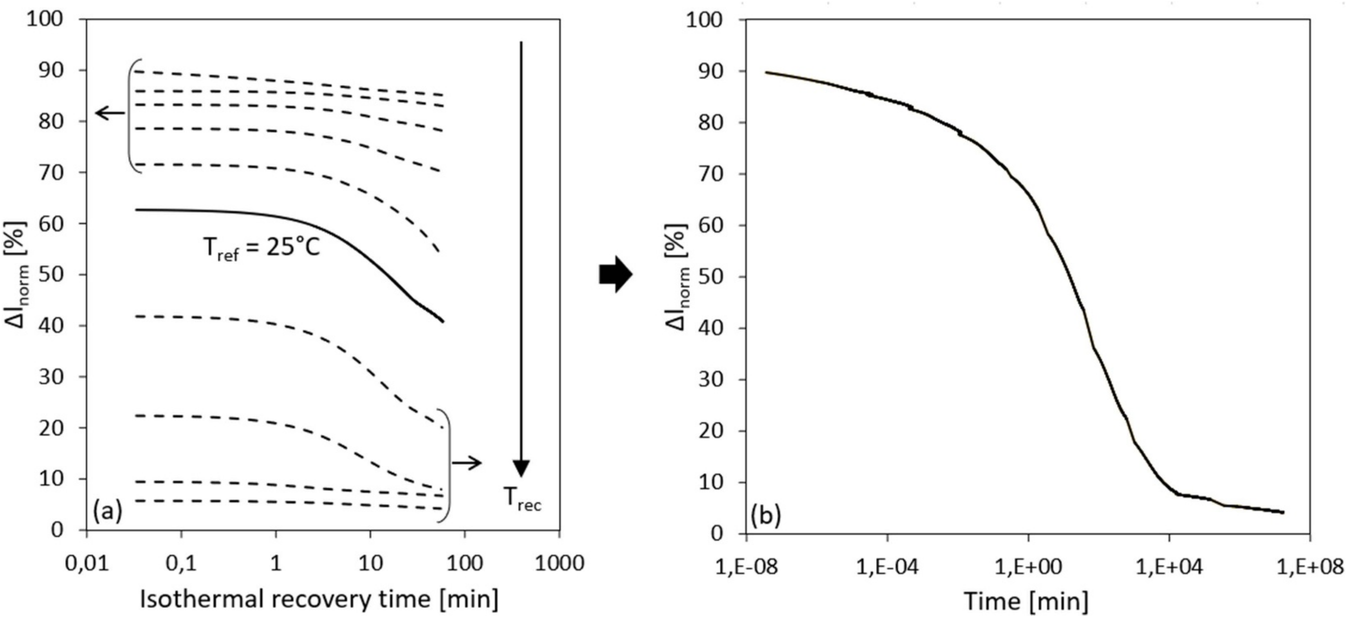

Figure 9. Construction of a recovery master curve (specimens programmed at T_{low}).

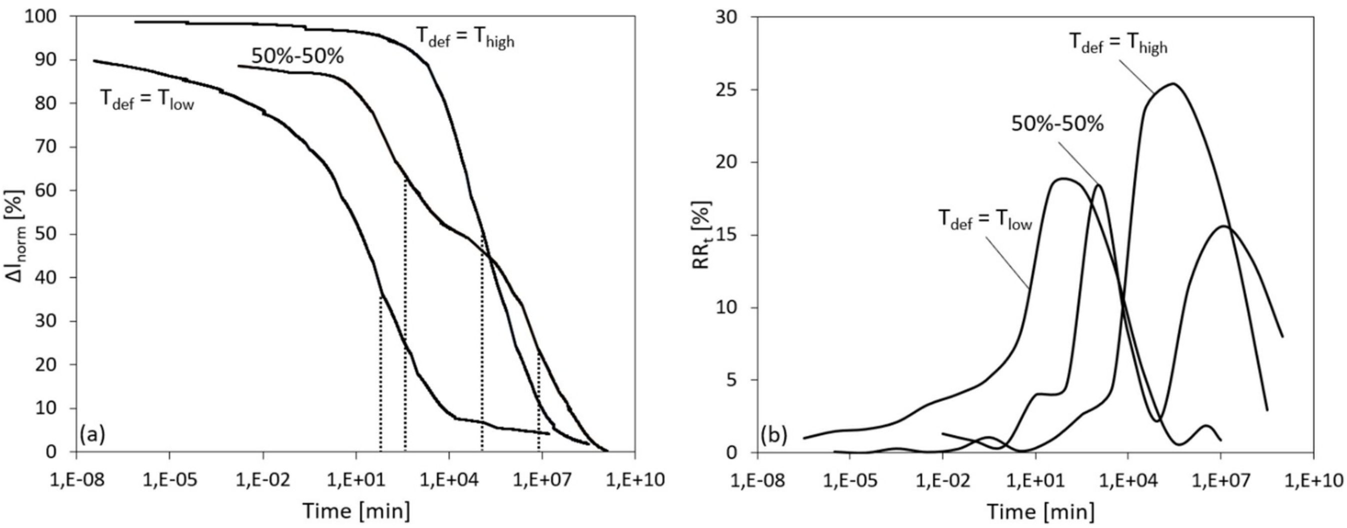

Figure 10. (a) Master curves of normalized displacement, Δl_{norm}, as a function of time for isothermal recovery tests performed on specimens deformed at T_{low}, at T_{high} or in two steps (50% at T_{low} and 50% at T_{high}), with reference temperature equal to 25 °C; (b) recovery rate, $\mathrm{RR_t}$, curves obtained from the normalized displacement master curves.

isothermal recovery processes. The recovery master curves describe the normalized displacement over the whole time scale, for a given reference temperature $T_0 = 25$ °C. Such master curves were built by rigidly shifting the isothermal curves along the time axis (i.e. isothermal recovery time values were divided by proper shift factors, $a_{T_0}^{T}$) until best superposition (figure 9). Curve segments obtained during the first minutes under isothermal conditions fell out of the main trend because they were still influenced by the previous (transient) heating ramp, therefore they were neglected for the final isothermal recovery master curves. The values of the shift factors are reported in figure S3, showing similar values for all three programming conditions and a trend similar also to that of shift factors from DMA master curves, though with a slightly less steep slope.

The resulting master curves are reported in figure 10(a), highlighting that, for the same reference temperature, specimens deformed at different temperatures showed a recovery process distributed along separated temporal regions. In particular, the isothermal recovery process was shifted towards longer times for specimens deformed at higher T_{def}. Moreover, considering the recovery rate peaks (figure 10(b)) as characteristic recovery times, the recovery processes of auxetic cells deformed at T_{low} (peak around 10^2 min) and at T_{high} (peak around 10^5 min) resulted separated by about three decades on the logarithmic time scale (i.e. specimens programmed at

Table 2. Prony parameters from DMA data fit.

i	τ_i	g_i	i	τ_i	g_i
1	2.81×10^{-13}	3.69×10^{-2}	12	1.84×10^{-1}	5.86×10^{-2}
2	4.36×10^{-12}	2.34×10^{-2}	13	6.18×10^{-1}	2.60×10^{-2}
3	1.15×10^{-10}	4.47×10^{-2}	14	2.49×10^{0}	7.43×10^{-2}
4	4.42×10^{-9}	4.19×10^{-2}	15	2.99×10^{1}	1.04×10^{-1}
5	5.35×10^{-8}	3.53×10^{-2}	16	4.33×10^{2}	6.53×10^{-2}
6	7.52×10^{-7}	6.07×10^{-2}	17	2.28×10^{3}	5.99×10^{-2}
7	1.15×10^{-5}	3.58×10^{-2}	18	2.63×10^{4}	4.61×10^{-2}
8	1.00×10^{-4}	6.87×10^{-2}	19	2.35×10^{5}	4.25×10^{-2}
9	1.29×10^{-3}	6.33×10^{-2}	20	6.05×10^{6}	1.49×10^{-2}
10	1.14×10^{-2}	6.37×10^{-2}	21	9.78×10^{7}	3.08×10^{-3}
11	5.37×10^{-2}	2.55×10^{-2}	22	2.29×10^{8}	1.00×10^{-4}

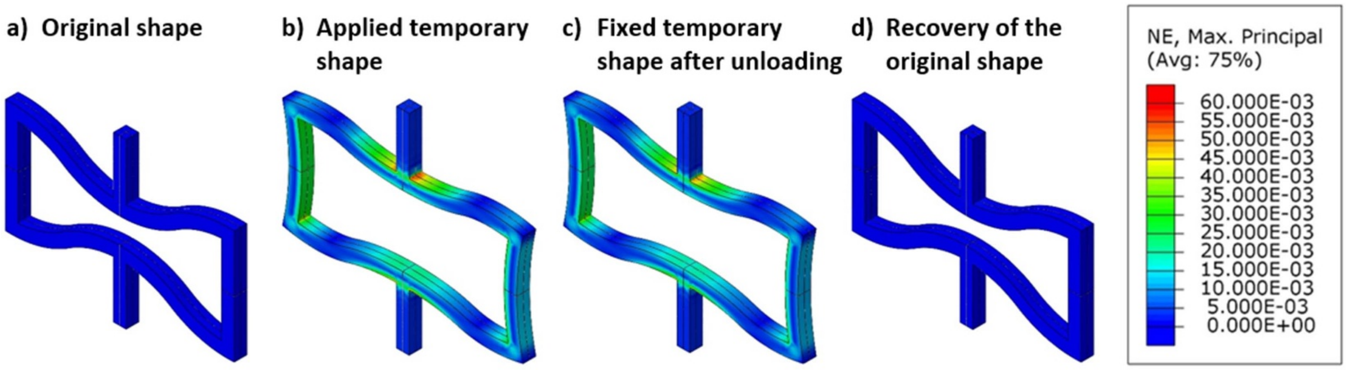

Figure 11. FE maps of the maximum principal strain for a single auxetic cell during a shape memory history: in its original shape (a), in its temporary shape at the maximum applied displacement (b), after unloading (c) and after recovery (d).

100 °C recovered their original shape over a time period a thousand times longer than specimens programmed at 40 °C).

In addition, it is noteworthy to remark that, although this separation of the two master curves on the time is shown for curves at a reference temperature $T_0 = 25$ °C, a similar separation is expected at any recovery temperature. In fact, the similar shift factor values obtained from the construction of both master curves would determine a same rigid shift of the curves along the time axis, whatever the temperature chosen as reference.

As for the sequential recovery, some difficulties were encountered in the isothermal curves superposition. On the master curve, two distinct recovery steps of about 50% each were observed and their presence was further highlighted in figure 10(b), where two separate recovery rate peaks could be distinguished. These recovery rate peaks were also aligned with a reasonable approximation to those found for the single-step processes. The second recovery step characteristic time appeared longer than the one identified for cells deformed at T_{high}, leading to a four-decade separation between recovery rate peaks. Nevertheless, the master curve trend was overall consistent with the other two and proved the possibility to program sequential motions that are distinctly separated on the time scale by simply applying multiple deformation steps at different temperatures.

3.4. Comparison between simulation results and experimental data

The shape memory experiments were simulated using the data obtained from the multifrequency DMA test for the FE model calibration. The value of G_∞ in the hyperelastic strain energy function was measured to be about 7.4 MPa, while the value of G_0 in the generalized Maxwell model was evaluated as 1283 MPa. Table 2 reports the optimal (g_i, τ_i) values resulted from the fitting of the master curve. Finally, the WLF parameters were evaluated as: (a) $C_1 = 39.3$ and $C_2 = 274.1$ °C when considering the shift factors employed in the construction of the master curve from DMA data; (b) $C_1 = 54.6$ and $C_2 = 451.5$ °C when considering the best fit of all the shift factors vs. $1/T$ curves obtained from isothermal recovery tests, grouped together as subtending a common trend.

FE maps of the maximum principal strain are briefly reported in figure 11 for the main steps of the shape memory cycle of a single auxetic cell. Quite clearly, the cell deformation mode was almost pure bending, with the cell struts acting as curved slender beams fixed together. A slight stress concentration along the cell thickness at the base of the struts used for load application can also be appreciated due to the notch effect. A very small elastic recoil could be appreciated when load is removed, as seen by comparing strain values of figure 11(b)

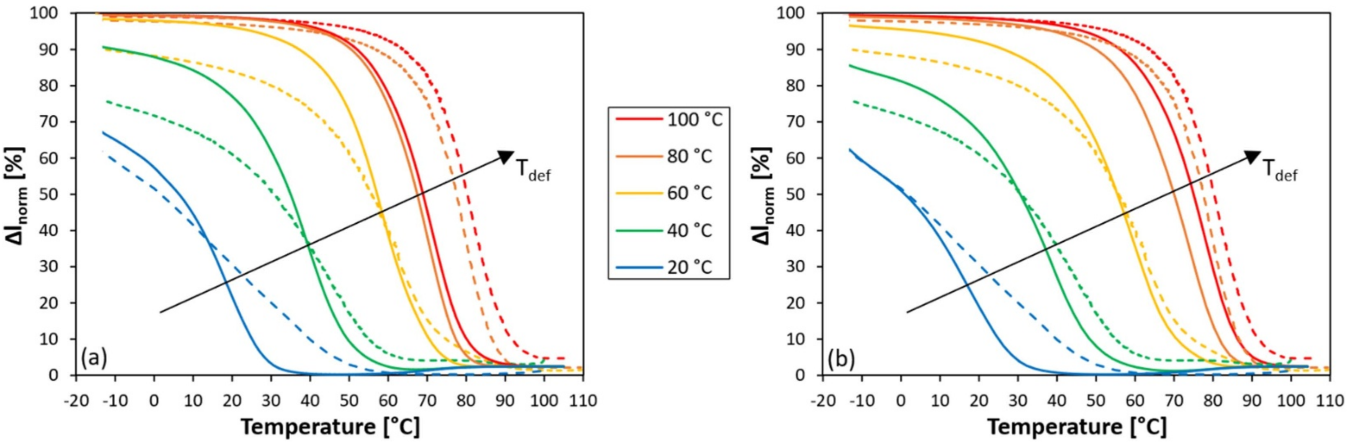

Figure 12. Comparison between experimental (dashed line) and simulated (solid line) single-step TSR curves. Simulation results were obtained with two different sets of WLF parameters: (a) WLF parameters derived from DMA; (b) WLF parameters derived from recovery master curves.

to those of figure 11(c), even though no significant displacement occurred, since unloading is carried out well below T_g. In terms of strain distribution, the typical bending strain gradients were localized in the central region when considering the cell width (i.e. along the longer side), while they were nearly homogenous on the whole struts when considering the cell height (i.e. the shorter side). Due to the cell struts being thin and almost purely bent, the peak principal strain values were mostly limited below 2.5% even with a noticeable opening of the cell.

Single-step TSR tests were first simulated using the WLF parameters derived from the shift factors employed in the construction of the master curve from DMA data. Figure 12(a) compares the results of these simulations with experimental ones, under a common representation as normalized displacement vs. temperature curves and for all the deformation temperatures applied ($T_{def} = 20 \div 100$ °C). Simulations provided an overall good qualitative prediction of the expected TSR curves, depicting both the good shape memory behavior of the material for all the deformation temperatures (i.e. high strain recovery values) and the two effects of the deformation temperature on the following recovery, i.e. the fact that higher T_{def} values enhance SF and shift the whole recovery process towards higher temperatures. However, on a quantitative point of view the model predictions differ from experimental results mainly in two respects: (a) for T_{def} up to 60 °C (i.e. well inside the glass transition region), the simulated recovery process occurred around the same temperature as the experimental one, but covered a narrower temperature range and began with higher SF values; (b) for T_{def} values at the upper limit of the glass transition region (80 °C) and beyond (100 °C), predicted curves displayed similar trends as the experimental ones but appeared shifted towards lower temperatures by about 10 °C.

These discrepancies are thought to be related to the difference among the time-temperature correlations between shift factors obtained by DMA data and those with a slightly less steep trend obtained by strain recovery master curves, as shown in figure S3. Therefore, in order to reduce the differences between FE modeling and reality, a different set of

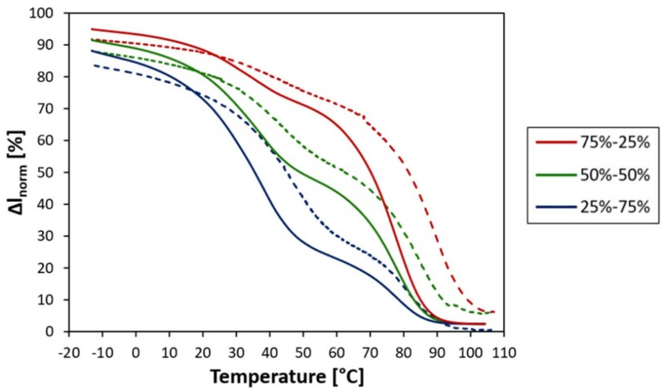

Figure 13. Comparison between experimental (dashed line) and simulated (solid line) double-step TSR curves; WLF parameters for simulations were derived from recovery master curves.

WLF parameters was calculated from the shift factors values used in the construction of recovery master curves. As shown in figure 12(b), this solution brought SF values closer to the experimental ones, broadened the recovery process distribution of specimens deformed at lower temperatures and shifted the curves of specimens deformed at 80 °C and 100 °C closer to the experimental ones. Therefore, this second method was identified as the most suitable to identify the correct parameters to describe temperature dependency with the WLF equation for the following shape memory test simulations.

The possibility to simulate sequential shape recovery histories was also investigated. The double-step programming conditions of the experimental tests were reproduced, applying 25%, 50% or 75% of the total deformation at $T_{high} = 100$ °C and the remaining part at $T_{low} = 40$ °C, and the results were plotted as normalized displacement against temperature in figure 13, together with the experimental curves.

The simulation of the double-step recovery process also seemed to adequately describe the experimental findings. In particular, the presence of the two inflection points and the amounts of strain recovered in each sub-process were well

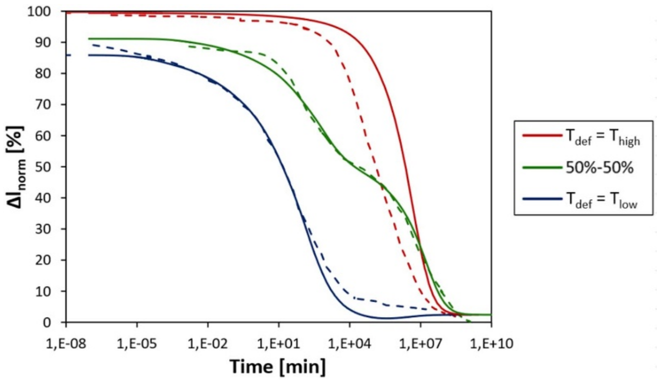

Figure 14. Comparison between experimental recovery master curves (dashed line), referred to $T_0 = 25$ °C, and simulated isothermal curves (solid line), obtained by simulation of complete shape recovery at 25 °C; WLF parameters for simulations were derived from recovery master curves.

captured by the model, as well as the increasing trend of SF values with the percentage of deformation applied at T_{high}. By contrast, the model failed in precisely determine the exact temperature at which each sub-step takes place; in fact, by taking the inflection points of the curves as reference, the corresponding recovery process was shifted of about 5 °C–15 °C towards lower temperatures. However, noteworthily, the FE model allows simulating sequential recovery histories, as proved by the presence of two well separated steps in the curves, and correctly capturing the effect of variations in the programming conditions on the shape memory response. This suggests that the model can be successfully used to predict the behavior of the material for various programming and recovery histories, thus acting as a valuable tool for design and optimization of sequential motions.

Finally, the shape recovery of auxetic cells was also simulated under isothermal conditions, to provide a purely time-dependent numerical description of the recovery process, so to compare it with experimental results and verify the validity of the constitutive model in reproducing the recovery process distribution along the time scale. In fact, similarly to experimental analyses, numerical simulations of the TME have so far described the process only for continuous [57] or segmented [56, 57] thermal ramps, thus describing the response as a function of temperature, or as a function of time but only for a specific thermal history.

This study was carried out by means of long isothermal simulations, during which T_{rec} was maintained constant until complete recovery of the auxetic cells. The simulations were carried out maintaining the lowest value of T_{rec} for each programming history (−20 °C for single-step programming at T_{high} or T_{low}; −15 °C for double-step programming, i.e. 50% of deformation at T_{high} and 50% at T_{low}), in order to cover even the short-time region of the recovery curves referred to 25 °C. The obtained results were then reduced to a same reference temperature (25 °C) by means of the measured shift factors.

The results are represented in figure 14 in terms of normalized displacement vs. time, and compared with the experimental recovery master curves, for the same reference temperature. A good agreement between experimental and simulated curves could be observed with regard to single-step programming at T_{low} and double-step programming, whereas the recovery process distribution for cells deformed at T_{high}, beyond the glass transition region, was once again more difficult to be reproduced by the model. However, despite a separation of about one decade on the time scale between the curves related to T_{high}, the overall outcome of this last series of numerical simulations was well aligned with experimental results. In fact, the simulations well represented the effects of the deformation temperature on the recovery process distribution of the material at the reference temperature: increasing T_{def}, a higher percentage of deformation is fixed at shorter times and the whole process is shifted towards longer times. Moreover, for the double-step programming, the simulation curve well predicted the two sequential steps, with characteristic times comparable with those obtained with single-step programming histories and separated by about four decades on the time scale.

3.5. Sequential recovery of in-plane and out-of-plane deformations for an auxetic grid

Given the encouraging results achieved in shape memory tests on single auxetic cells subjected to simple tensile deformations, a more complex programming history was applied to a complete auxetic grid, so to test the TME occurrence and numerical model capability for more complex systems. In-plane and out-of-plane deformations were combined to obtain a 4D-printed object capable of sequential motions in response to a proper thermal stimulus: the grid was subjected to elongation at T_{high}, bending at T_{low} and heating along a thermal ramp up to about 63 °C, following the steps described in section 2.5. The employ of visually distinguishable in-plane and out-of-plane motions also served to better decouple, along a same heating ramp, the recovery of the two deformations applied. In fact, in most of the work in which the recovery of a multi-step deformation was studied along continuous heating ramps, the two recovery steps were partially overlapped in the terminal/onset regions [49, 57]. The only way to properly highlight different motions in the same sample along a same ramp is to deform the systems in different locations or with different deformation modes at different temperatures, as in [47, 48, 51].

The results of the experiment and of its numerical simulation are collected in figure 15, reporting selected pictures of the recovery as well as recovery curves of in-plane and out-of-plane deformations calculated via equations (10) and (11). Videos of the recovering structures and of the simulations results are reported as well as supplementary files (videos S1 and S2).

The pictures show the top view of the auxetic grid, as well as the top view and the side view of its CAD model, for increasing temperatures along the heating ramp. Most of the unfolding was observed within 40 °C, while the recovery of the elongation required higher temperatures, so that the two movements were successfully separated along the time scale. The temperature intervals covered by the two steps of the recovery process can be better identified in figure 15(e). In

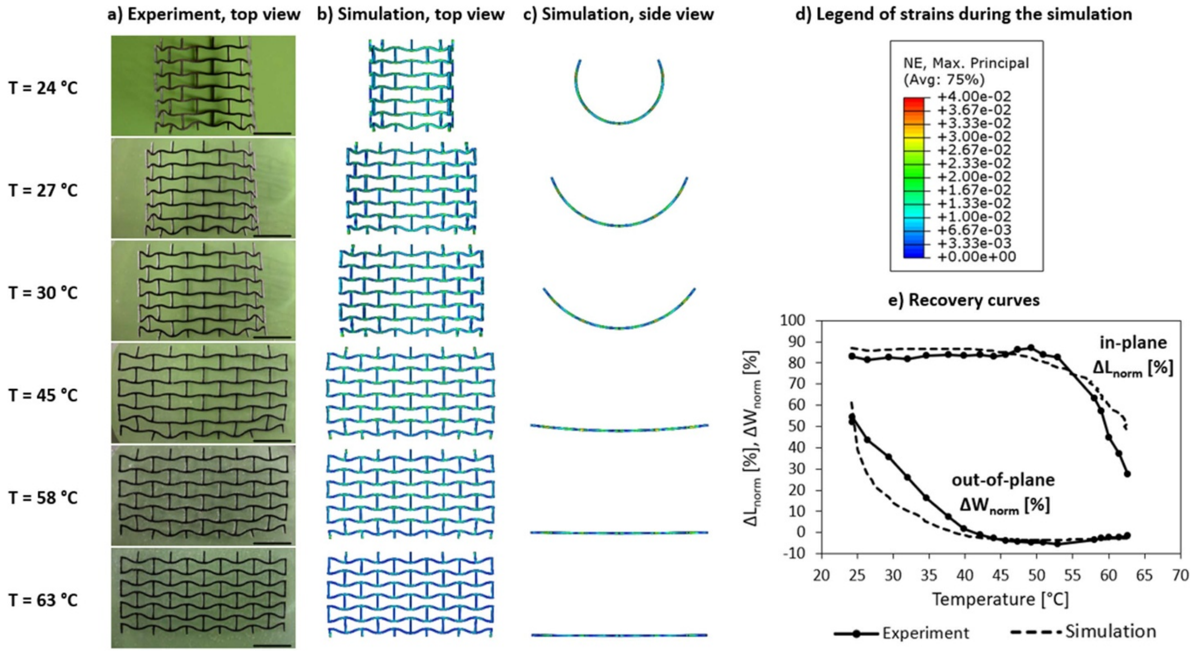

Figure 15. Experimental and simulated recovery of an auxetic grid along a heating ramp after double-step programming (tensile elongation at T_{high} and bending at T_{low}): (a) photographs of the experiment (the marker is 20 mm); (b)–(d) pictures of the simulation; (e) experimental and simulated recovery curves of in-plane and out-of-plane deformations.

terms of out-of-plane recovery at T_{low}, the simulated recovery took place in the same temperature range as the experimental one and both the SF at unloading and the residual deformation after recovery were well predicted. However, a faster recovery transient could be observed in the simulation, possibly due to both a non-ideal material behavior (e.g. the assumed material model is not a perfect fit) and some minor inaccuracies in the experimental procedure and FE modeling. In fact, the experimental control of thermal and deformation histories was not trivial and minor inaccuracies in the replication of boundary and loading condition are to be expected. Conversely, the recovery of the in-plane deformation at T_{high} appeared to be slower in the simulation. Again, this behavior was most likely due to both a non-ideal material and some experimental inaccuracies. In fact, it is reasonable to assume that the experimental temperature was slightly underestimated during the in-plane recovery, when the temperature gradient caused by thermal loads and boundary conditions is more significant. Nonetheless, the FE model proved to be a suitable instrument to predict the shape memory behavior of objects with complex structures and articulate programming histories.

Furthermore, this experiment can be considered as an interesting proof-of-concept towards the development of metamaterials capable of programmable shape-shifting sequences triggered by the temperature. In fact, adding the ability of a non-mechanical stimulus-responsiveness to structures that are capable of shape-morphing and show complex mechanical response may be of interest for the achievement of untethered structures with complex motions, e.g. in soft robotics and medical device development.

4. Conclusions

The shape memory behavior of auxetic structures obtained by AM of a commercial photopolymer resin was studied through TSR and isothermal recovery tests.

TSR experiments highlighted a good shape memory behavior and the peculiar TME of the photopolymer, as a consequence of its broad glass transition region. Exploiting the TME proved to be an effective method to tune the recovery process of the auxetic cells along the temperature scale by applying properly designed thermo-mechanical cycles. In particular, programming histories consisting of multiple steps carried out at distinct deformation temperatures allowed obtaining highly controlled sequential movements, without recurring to multi-material printing or complex macromolecular architectures. Moreover, isothermal recovery tests were employed to provide a master curve representation of the whole recovery process. This representation allowed better determining the distribution of the recovery process, as well as the characteristic recovery time, of variously programmed systems.

Numerical simulations of the experiments were carried out in order to investigate the possibility of describing the shape memory response of the auxetic cells with a thermo-viscoelastic model, which was calibrated on the data obtained from multifrequency DMA characterization. Experimental and simulated recovery curves exhibited fair correspondence, which was then improved by adjusting the model parameters describing the time-temperature correlation on the basis of isothermal recovery data. Simulations could replicate all the experiments, though the best predictions were obtained for isothermal recovery tests, and for TSR tests when the deformation temperatures were selected well within the glass transition region.

The acquired knowledge and the FE model can guide the development of 4D-printed objects characterized by complex geometry (e.g. auxetic patterns) and capable of complex shape transformations (e.g. sequential motions). In fact, great design freedom can be achieved with AM technologies, while shape recovery tunability can be obtained thanks to the TME of the resin and to the application of proper thermo-mechanical histories, based on the experience gained in this study and on the outcomes predictable through FE simulations.

As a proof-of-concept, the sequential shape transformation of an auxetic honeycomb grid was here realized and consistently simulated, decoupling in-plane and out-of-plane deformations on temperature and time scales. The fair correspondence between experimental and model results confirmed that the proposed FE approach may be a suitable tool for the design of shape memory objects with complex shapes and histories.

Data availability statement

All data that support the findings of this study are included within the article (and any supplementary files).

Acknowledgment

The authors kindly acknowledge Ms Marica Bianchi for her contribution to the shape memory characterization.

ORCID iDs

Chiara Pasini https://orcid.org/0000-0001-7478-239X
Nicoletta Inverardi https://orcid.org/0000-0003-3550-9299
Davide Battini https://orcid.org/0000-0002-2044-5985
Giulia Scalet https://orcid.org/0000-0001-7683-566X
Stefania Marconi https://orcid.org/0000-0003-4608-6180
Ferdinando Auricchio https://orcid.org/0000-0002-3735-2400
Stefano Pandini https://orcid.org/0000-0003-2390-8495

References

[1] Melly S K, Liu L, Liu Y and Leng J 2020 On 4D printing as a revolutionary fabrication technique for smart structures *Smart Mater. Struct.* **29** 083001
[2] Joshi S, Rawat K, C C K, Rajamohan V, Mathew A T, Koziol K, Kumar Thakur V and Balan A S S 2020 4D printing of materials for the future: opportunities and challenges *Appl. Mater. Today* **18** 100490
[3] Ding H, Zhang X, Liu Y and Ramakrishna S 2019 Review of mechanisms and deformation behaviors in 4D printing *Int. J. Adv. Manuf. Technol.* **105** 4633–49
[4] Momeni F, Mehdi M, Hassani. N S, Liu X and Ni J 2017 A review of 4D printing *Mater. Des.* **122** 42–79
[5] Tibbits S 2014 4D printing: multi-material shape change *Archit. Des.* **84** 116–21
[6] Tibbits S, McKnelly C, Olguin C, Dikovsky D and Hirsch S 2014 4D Printing and universal transformation *ACADIA 2014—Design Agency: Proc. 34th Annual Conf. Association for Computer Aided Design in Architecture* (*Los Angeles, 23–25 October 2014*) p 539
[7] Goo B, Hong C-H and Park K 2020 4D printing using anisotropic thermal deformation of 3D-printed thermoplastic parts *Mater. Des.* **188** 108485
[8] Rajkumar A R and Shanmugam K 2018 Additive manufacturing-enabled shape transformations via FFF 4D printing *J. Mater. Res.* **33** 4362–76
[9] Kolken H M A and Zadpoor A A 2017 Auxetic mechanical metamaterials *RSC Adv.* **7** 5111–29
[10] Ren X, Das R, Tran P, Ngo T D and Xie Y M 2018 Auxetic metamaterials and structures: a review *Smart Mater. Struct.* **27** 023001
[11] Prawoto Y 2012 Seeing auxetic materials from the mechanics point of view: a structural review on the negative Poisson's ratio *Comput. Mater. Sci.* **58** 140–53
[12] Saxena K K, Das R and Calius E P 2016 Three decades of auxetics research—materials with negative Poisson's ratio: a review *Adv. Eng. Mater.* **18** 1847–70
[13] Liu Q 2006 Literature review: materials with negative poisson's ratios and potential applications to aerospace and defence *Aust. Gov. Dep. Def.* (available at: http://apps.dtic.mil/sti/pdfs/ADA460791.pdf)
[14] Sanami M, Ravirala N, Alderson K and Alderson A 2014 Auxetic materials for sports applications *Proc. Eng.* **72** 453–8
[15] Zhang S L, Lai Y-C, He X, Liu R, Zi Y and Wang Z L 2017 Auxetic foam-based contact-mode triboelectric nanogenerator with highly sensitive self-powered strain sensing capabilities to monitor human body movement *Adv. Funct. Mater.* **27** 1606695
[16] Alderson A, Rasburn J, Ameer-Beg S, Mullarkey P G, Perrie W and Evans K E 2000 An auxetic filter: a tuneable filter displaying enhanced size selectivity or defouling properties *Ind. Eng. Chem. Res.* **39** 654–65
[17] Ali M N, Busfield J J C and Rehman I U 2014 Auxetic oesophageal stents: structure and mechanical properties *J. Mater. Sci. Mater. Med.* **25** 527–53
[18] Bhullar S K, Ko J, Ahmed F and Jun M 2014 Design and fabrication of stent with negative Poisson's ratio *Int. J. Mech. Ind. Sci. Eng.* **8** 448–54
[19] Alderson A and Alderson K 2005 Expanding materials and applications: exploiting auxetic textiles *Tech. Text. Int.* **14** 29–34
[20] Alderson K, Alderson A, Anand S, Simkins V, Nazare S and Ravirala N 2012 Auxetic warp knit textile structures *Phys. Status Solidi* b **249** 1322–9
[21] Simkins V R, Alderson A, Davies P J and Alderson K L 2005 Single fibre pullout tests on auxetic polymeric fibres *J. Mater. Sci.***40** 2829–3
[22] Sun Y and Pugno N 2013 Hierarchical fibers with a negative Poisson's ratio for tougher composites *Materials* **6** 699–712
[23] Choi J B and Lakes R S 1991 Design of a fastener based on negative Poisson's ratio foam *Cell. Polym.* **10** 205–12
[24] Ren X, Shen J, Tran P, Ngo T D and Xie Y M 2018 Auxetic nail: design and experimental study *Compos. Struct.* **184** 288–98
[25] Bertoldi K, Vitelli V, Christensen J and Van Hecke M 2017 Flexible mechanical metamaterials *Nat. Rev. Mater.* **2** 17066
[26] Lakes R S 2017 Negative-Poisson's-ratio materials: auxetic solids *Annu. Rev. Mater. Res.* **47** 63–81
[27] Wang Z, Luan C, Liao G, Liu J, Yao X and Fu J 2020 Progress in auxetic mechanical metamaterials: structures, characteristics, manufacturing methods, and applications *Adv. Eng. Mater.* **22** 2000312

[28] Clausen A, Wang F, Jensen J S, Sigmund O and Lewis J A 2015 Topology optimized architectures with programmable Poisson's ratio over large deformations *Adv. Mater.* **27** 5523–7

[29] Whitty J P M, Nazare F and Alderson A 2002 Modelling the effects of density variations on the in-plane Poisson's ratios and Young's moduli of periodic conventional and re-entrant honeycombs—part 1: rib thickness variations *Cell. Polym.* **21** 69–98

[30] Mizzi L, Grima J N, Gatt R and Attard D 2019 Analysis of the deformation behavior and mechanical properties of slit-perforated auxetic metamaterials *Phys. Status Solidi* b **256** 1800153

[31] Masters I G and Evans K E 1996 Models for the elastic deformation of honeycombs *Compos. Struct.* **35** 403–22

[32] Lei M, Hong W, Zhao Z, Hamel C, Chen M, Lu H and Qi H J 2019 3D printing of auxetic metamaterials with digitally reprogrammable shape *ACS Appl. Mater. Interfaces* **11** 22768–76

[33] Yousuf M H, Abuzaid W and Alkhader M 2020 4D printed auxetic structures with tunable mechanical properties *Addit. Manuf.* **35** 101364

[34] Xin X, Liu L, Liu Y and Leng J 2020 4D printing auxetic metamaterials with tunable, programmable, and reconfigurable mechanical properties *Adv. Funct. Mater.* **30** 2004226

[35] Bodaghi M and Liao W H 2019 4D printed tunable mechanical metamaterials with shape memory operations *Smart Mater. Struct.* **28** 045019

[36] Wan M, Yu K and Sun H 2022 4D printed programmable auxetic metamaterials with shape memory effects *Compos. Struct.* **279** 114791

[37] Ren L, Wu W, Ren L, Song Z, Liu Q, Li B, Wu Q and Zhou X 2022 3D printing of auxetic metamaterials with high-temperature and programmable mechanical properties *Adv. Mater. Technol.* 2101546c

[38] Wei Y-L, Yang Q-S and Tao R 2021 SMP-based chiral auxetic mechanical metamaterial with tunable bandgap function *Int. J. Mech. Sci.* **195** 106267

[39] Li Z, Liu Y, Wang Y, Lu H, Lei M and Fu Y Q 2021 3D printing of auxetic shape-memory metamaterial towards designable buckling *Int. J. Appl. Mech.* **13** 2150011

[40] Jebellat E, Baniassadi M, Moshki A, Wang K and Baghani M 2020 Numerical investigation of smart auxetic three-dimensional meta-structures based on shape memory polymers via topology optimization *J. Intell. Mater. Syst. Struct.* **31** 1838–52

[41] Wagner M, Chen T and Shea K 2017 Large shape transforming 4D auxetic structures *3D Print. Addit. Manuf.* **4** 133–42

[42] Bodaghi M, Serjouei A, Zolfagharian A, Fotouhi M, Rahman H and Durand D 2020 Reversible energy absorbing meta-sandwiches by FDM 4D printing *Int. J. Mech. Sci.* **173** 105451

[43] Kabir S and Lee S 2020 Study of shape memory and tensile property of 3D printed sinusoidal sample/nylon composite focused on various thicknesses and shape memory cycles *Polymers* **127** 1600

[44] Miaudet P, Derré A, Maugey M, Zakri C, Piccione P M, Inoubli R and Poulin P 2007 Shape and temperature memory of nanocomposites with broadened glass transition *Science* **318** 1294–6

[45] Xie T 2010 Tunable polymer multi-shape memory effect *Nature* **464** 267–70

[46] Yu K, Dunn M L and Qi H J 2015 Digital manufacture of shape changing components *Extreme Mech. Lett.* **4** 9–17

[47] Inverardi N, Pandini S, Bignotti F, Scalet G, Marconi S and Auricchio F 2020 Sequential motion of 4D printed photopolymers with broad glass transition *Macromol. Mater. Eng.* **305** 1900370

[48] Pandini S, Inverardi N, Scalet G, Battini D, Bignotti F, Marconi S and Auricchio F 2020 Shape memory response and hierarchical motion capabilities of 4D printed auxetic structures *Mech. Res. Commun.* **103** 103463

[49] Xie T, Page K A and Eastman S A 2011 Strain-based temperature memory effect for Nafion and its molecular origins *Adv. Funct. Mater.* **21** 2057–66

[50] Wang Y, Li J, Li X, Pan Y, Zheng Z, Ding X and Peng Y 2014 Relation between temperature memory effect and multiple-shape memory behaviors based on polymer networks *RSC Adv.* **4** 20364–70

[51] Kratz K, Madbouly S A, Wagermaier W and Lendlein A 2011 Temperature-memory polymer networks with crystallizable controlling units *Adv. Mater.* **23** 4058–62

[52] Behl M, Kratz K, Noechel U, Sauter T and Lendlein A 2013 Temperature-memory polymer actuators *Proc. Natl Acad. Sci. USA* **110** 12555–9

[53] Fritzsche N and Pretsch T 2014 Programming of temperature-memory onsets in a semicrystalline polyurethane elastomer *Macromolecules* **47** 5952–9

[54] Mirtschin N and Pretsch T 2015 Designing temperature-memory effects in semicrystalline polyurethane *RSC Adv.* **5** 46307–15

[55] Wang L, Di S, Wang W, Chen H, Yang X, Gong T and Zhou S 2014 Tunable temperature memory effect of photo-cross-linked star PCL-PEG networks *Macromolecules* **47** 1828–36

[56] Yu K, Xie T, Leng J, Ding Y and Qi H J 2012 Mechanisms of multi-shape memory effects and associated energy release in shape memory polymers *Soft Matter* **8** 5687–95

[57] Xiao R, Guo J and Nguyen T D 2015 Modeling the multiple shape memory effect and temperature memory effect in amorphous polymers *RSC Adv.* **5** 416–23

[58] Ge Q, Dunn C K, Qi H J and Dunn M L 2014 Active origami by 4D printing *Smart Mater. Struct.* **23** 094007

[59] Mao Y, Yu K, Isakov M S, Wu J, Dunn M L and Jerry Q H 2015 Sequential self-folding structures by 3D printed digital shape memory polymers *Sci. Rep.* **5** 13616

[60] Yu K, Ritchie A, Mao Y, Dunn M L and Qi H J 2015 Controlled sequential shape changing components by 3D printing of shape memory polymer multimaterials *Proc. IUTAM* **12** 193–203

[61] Chen T, Bilal O R, Shea K and Daraio C 2018 Harnessing bistability for directional propulsion of soft, untethered robots *Proc. Natl Acad. Sci. USA* **115** 5698–702

[62] Diorio A M, Luo X, Lee K M and Mather P T 2010 A functionally graded shape memory polymer *Soft Matter* **7** 68–74

[63] Pei E, Loh G H, Harrison D, De Amorim Almeida H, Verona M D M and Paz R 2017 A study of 4D printing and functionally graded additive manufacturing *Assem. Autom.* **37** 147–53

[64] Hassan R U, Jo S and Seok J 2018 Fabrication of a functionally graded and magnetically responsive shape memory polymer using a 3D printing technique and its characterization *J. Appl. Polym. Sci.* **135** 45997

[65] Zhao J, Chen M, Wang X, Zhao X, Wang Z, Dang Z-M, Ma L, Hu G-H and Chen F 2013 Triple shape memory effects of cross-linked polyethylene/polypropylene blends with cocontinuous architecture *ACS Appl. Mater. Interfaces* **5** 5550–6

[66] Lai S-M, You P-Y, Chiu Y T and Kuo C W 2017 Triple-shape memory properties of thermoplastic polyurethane/olefin block copolymer/polycaprolactone blends *J. Polym. Res.* **24** 161

[67] Peng B, Yang Y, Gu K, Amis E J and Cavicchi K A 2019 Digital light processing 3D printing of triple shape memory polymer for sequential shape shifting *ACS Mater. Lett.* **1** 410–7
[68] Zhang C, Gou X and Xiao R 2018 Controllable shape-memory recovery regions in polymers through mechanical programming *J. Appl. Polym. Sci.* **135** 45909
[69] Yu K and Qi H J 2014 Temperature memory effect in amorphous shape memory polymers *Soft Matter* **10** 9423–32
[70] Pandini S, Avanzini A, Battini D, Berardi M, Baldi F and Bignotti F 2016 Shape memory behavior of epoxy-based model materials: tailoring approaches and thermo-mechanical modeling *AIP Conf. Proc.* **1736** 020175
[71] Arrieta J S, Diani J and Gilormini P 2014 Experimental and modelling studies of the shape memory properties of amorphous polymer network composites *Smart Mater. Struct.* **23** 095009
[72] Diani J, Gilormini P, Frédy C and Rousseau I 2012 Predicting thermal shape memory of crosslinked polymer networks from linear viscoelasticity *Int. J. Solids Struct.* **49** 793–9
[73] Arrieta S, Diani J and Gilormini P 2014 Experimental characterization and thermoviscoelastic modeling of strain and stress recoveries of an amorphous polymer network *Mech. Mater.* **68** 95–103
[74] Kuki Á, Czifrák K, Karger-Kocsis J, Zsuga M and Kéki S 2015 An approach to predict the shape-memory behavior of amorphous polymers from dynamic mechanical analysis (DMA) data *Mech. Time Depend. Mater.* **19** 87–93
[75] Ghobadi E, Sivanesapillai R, Musialak J and Steeb H 2016 Modeling based characterization of thermorheological properties of polyurethane ESTANE ™ *Int. J. Polym. Sci.* **2016** 7514974
[76] Christensen R M 1982 *Theory of Viscoelasticity : An Introduction* 2nd edn (Amsterdam: Elsevier)
[77] Bergström J 2015 Linear viscoelasticity *Mechanics of Solid Polymers: Theory and Computational Modeling* (Amsterdam: Elsevier) pp 309–51
[78] Park S W and Schapery R A 1999 Methods of interconversion between linear viscoelastic material functions. Part I—a numerical method based on Prony series *Int. J. Solids Struct.* **36** 1653–75
[79] Battini D, Avanzini A, Pandini S and Bignotti F 2020 Modeling approach and finite element analyses of a shape memory epoxy-based material *Proc. 24th AIMETA Conf. 2019* (*Lecture Notes in Mechanical Engineering*) pp 689–704